Lamina Cribrosa Pore Shape and Size as Predictors of Neural Tissue Mechanical Insult

Andrew P. Voorhees,[1] Ning-Jiun Jan,[1,2] Morgan E. Austin,[2] John G. Flanagan,[3] Jeremy M. Sivak,[4] Richard A. Bilonick,[1] and Ian A. Sigal[1,2]

[1]Department of Ophthalmology, University of Pittsburgh, Pittsburgh, Pennsylvania, United States
[2]Department of Bioengineering, University of Pittsburgh, Pittsburgh, Pennsylvania, United States
[3]Optometry and Vision Science, University of California Berkeley, Berkeley, California, United States
[4]Ophthalmology and Vison Sciences, University of Toronto, Toronto, Ontario, Canada

Correspondence: Ian A. Sigal, Ocular Biomechanics Laboratory, Department of Ophthalmology, University of Pittsburgh School of Medicine, 203 Lothrop Street, Room 930, Pittsburgh, PA 15213, USA; Ian@OcularBiomechanics.com.

Submitted: April 8, 2017
Accepted: September 14, 2017

Citation: Voorhees AP, Jan N-J, Austin ME, et al. Lamina cribrosa pore shape and size as predictors of neural tissue mechanical insult. *Invest Ophthalmol Vis Sci*. 2017;58:5336–5346. DOI: 10.1167/iovs.17-22015

Purpose. The purpose of this study was to determine how the architecture of the lamina cribrosa (LC) microstructure, including the shape and size of the lamina pores, influences the IOP-induced deformation of the neural tissues within the LC pores using computational modeling.

Methods. We built seven specimen-specific finite element models of LC microstructure with distinct nonlinear anisotropic properties for LC beams and neural tissues based on histological sections from three sheep eyes. Changes in shape (aspect ratio and convexity) and size (area and perimeter length) due to IOP-induced hoop stress were calculated for 128 LC pores. Multivariate linear regression was used to determine if pore shape and size were correlated with the strain in the pores. We also compared the microstructure models to a homogenized model built following previous approaches.

Results. The LC microstructure resulted in focal tensile, compressive, and shear strains in the neural tissues of the LC that were not predicted by homogenized models. IOP-induced hoop stress caused pores to become larger and more convex; however, pore aspect ratio did not change consistently. Peak tensile strains within the pores were well predicted by a linear regression model considering the initial convexity (negative correlation, $P < 0.001$), aspect ratio (positive correlation, $P < 0.01$), and area (negative correlation, $P < 0.01$). Significant correlations were also found when considering the deformed shape and size of the LC pores.

Conclusions. The deformation of the LC neural tissues was largely dependent on the collagenous LC beams. Simple measures of LC pore shape and area provided good estimates of neural tissue biomechanical insult.

Keywords: lamina cribrosa, optic nerve head, biomechanics, glaucoma, microstructure, finite element modeling, intraocular pressure, convexity

The lamina cribrosa (LC) is a complex tissue consisting of an intricate network of collagenous beams and blood vessels that support the delicate neural tissues as they exit the eye.[1,2] The LC is the site of initial glaucomatous damage, and it is widely postulated that retinal ganglion cell (RGC) loss is, in large part, due to mechanical insult to their axons within the LC.[2–7] This may be through compression or shearing of the RGC axons reducing axoplasmic transport,[4,8] stretch-induced activation of astrocytes,[9–12] or disruption of the vasculature leading to ischemia.[8,12–14] The response to elevated IOP varies from individual to individual, with some patients developing glaucoma at low IOPs and others maintaining normal vision despite elevated IOP. The underlying causes for these variations remain unclear. A hypothesis has been that these differences are explained by the organization of the LC microstructure and in particular, the shape and size of the laminar pores.[8,15–20]

Several investigations have examined LC pore shape and size in vivo[16–19,21–26] and ex vivo.[27,28] However, the findings of these studies have been mixed and a consensus conclusion has not been reached as to which pore characteristics are correlated with glaucoma status or progression. A major challenge of these studies has been that they have generally been unable to measure the IOP-induced mechanical insult and the acute changes in pore shape and size that result. Mechanical modeling offers an alternative approach for testing and understanding the association between pore properties and the potential for glaucomatous neuropathy due to mechanical insult.

Resolving the effects of pore shape requires models that explicitly incorporate the microstructure of the LC, something that the vast majority of previous LC models have not done. Instead, most models have treated the LC as a homogenized mixture of neural tissues and connective tissue.[20,29–31] This was, in part, because of the limited availability of high-resolution data on the collagen microarchitecture of the LC. We have recently developed and reported on microstructure-specific models based on high-resolution polarized light images that allows us to distinguish between the load-bearing, stiff, laminar beams and the frail, compliant, neural tissues of the LC.[32] The goal of this study was to leverage these microstructure-based models to determine if the shape and size of LC

pores predicts the biomechanical insult within the neural tissues of the pores due to IOP-induced hoop stress.

This study is organized into three parts. First, we used our models to test the role of the LC microstructure. We did this by comparing our microstructure models to a homogenized model built using approaches that have been previously reported.[29,31] Second, we used multivariate linear regression to determine if there were correlations between LC pore shape and size and the level of neural tissue strain resulting from the hoop stress caused by elevated IOP. Last, we examined how the shape of the pores changed with IOP-induced hoop stress and if the changes made them more robust or more susceptible to insult.

Methods

Modeling

This study is a further analysis of the modeling data set we recently reported on, and a detailed description of the methodology, assumptions, and limitations can be found therein.[32] A pictorial overview of our multiscale modeling method is presented in Figures 1 and 2. Briefly, our models were constructed from data obtained from histological sections of sheep optic nerve heads (ONH) imaged using polarized light microscopy,[33,34] and the details of the histology and imaging pertinent to this study can be found in our recent report.[32] Although these data provided excellent high-resolution information on the structure and orientation of the collagen fibers of the ONH, the information was only two-dimensional (2D). Hence, our models consider only a planar section of the ONH and our boundary conditions only consider the effects of the hoop-stress induced by elevated IOP. Given that previous studies have estimated the magnitude of IOP-induced hoop stress to be 10 to 30 times the magnitude of IOP itself,[29,32] we reasoned that IOP-induced hoop-stress is a primary mechanical insult resulting from IOP. Nonetheless, our models do not consider the posterior bowing of the lamina caused by the direct application of IOP to the LC and scleral surface. Discussions on the strengths and weaknesses of this approach can be found in our previous study,[32] and in a report from Zhang and colleagues,[29] who used a similar approach to study the effects of collagen organization in the ONH.

Mesoscale Models for Determining Boundary Conditions. As detailed in Figure 1 and described previously in full details,[32] we first created models of the ONH at a mesoscale level to use as boundary conditions for microscale models of portions of the LC. In total, three mesoscale models were made, one for each eye included in the study. For each eye, 6 to 10 serial histological sections were obtained from sheep eyes fixed in formalin at an IOP of 5 mm Hg, imaged with polarized light microscopy at a resolution of 4.4 μm,[32–34] and registered to one another. The average pixel energy, a measure of collagen density, and the average pixel orientation for the set of images was calculated for use as the basis for the mesoscale models.[34] For the mesoscale models, our geometric approach was similar to the one presented by Zhang et al.[29]; however, we modeled the ONH and surrounding sclera as a circular disk rather than a square. Quadratic tetrahedral elements with an average edge length of 112 μm were used for each mesoscale model. ONH tissue was modeled as a fiber-reinforced composite with fibers modeled using an exponential power law and ground substance modeled as a Neo-Hookean solid. Our approach to the material properties was similar to the one employed by Campbell et al.[20] in which the strain energy density for our collagenous tissue was weighted by the density of the collagen fibers, which we determined using polarized light microscopy. With this approach, the strain energy of the fibers varied linearly with collagen density. The weighting was chosen such that any element with an average pixel energy value equal to the average pixel energy value of all elements belonging to the sclera had material properties matching the properties that were based on previously reported measurements for human scleral collagen (Table 1). The preferred fiber orientation for our models also came from our specimen-specific measurements of collagen fiber orientation. A von Mises distribution was used to model the angular distribution of collagen fibers. However, we did not use direct measurements of the collagen fiber distribution. Instead we chose a fiber dispersion factor of 0.6 as this was found to be a reasonable estimate in the study from which we obtained our material properties for scleral colllagen.[35] To simulate the effects of IOP, a uniform outward boundary pressure was applied to the edges of the disk to mimic the effects of hoop stress as done by Zhang et al.[29] Based on the Law of Laplace, we determined that the hoop stress multiplier for sheep eyes was 10× IOP. Thus, to model an IOP increase of 30 mm Hg, an outward boundary pressure of 300 mm Hg was applied (39.9 kPa).

Microscale Modeling of LC Microstructure. For the microscale models (Fig. 2), seven regions (~0.3–0.9 mm^2) with clearly defined collagen beams and no evidence of histological artifacts such as missing tissue or section folds were selected for study. Four of these regions were taken from central LC and three regions from the peripheral LC, which included the scleral boundary. For the microscale models, sections were imaged at a resolution of 0.73 μm per pixel, and the images were registered to the images used to create the mesoscale models. Collagen density was used as the basis for 2D image segmentation. An intensity-based threshold was used to segment the collagen beams and the neural tissue pores. Segmented masks were edited manually to correct for local defects including those due to the presence of pigment. Small beams that were unconnected on one end were added to the neural tissues to avoid potential artifacts. From the 2D-segmented image, a three-dimensional (3D) reconstruction of the LC microstructure and neural tissue was created by assuming that the LC beams had a circular cross-section. Elsewhere we have demonstrated that this approach is more realistic than the simpler alternative of assuming that the LC beams have square cross-sections.[32] Our circular beam reconstruction method produced a model that was symmetric about the coronal plane (Fig. 2, top right), and thus the deformation was also assumed to be symmetric about this plane. This allowed us to model only half of the reconstructed LC volume. The LC beams and neural tissues were modeled using a quadratic tetrahedral mesh. The mean fiber orientation for each LC beam element was determined by nearest neighbor interpolation from the polarized light microscopy fiber orientation data. Material properties for the LC beams were the same as those used in the mesoscale models, which were based on the properties of human sclera (Table 1). The properties of the neural tissue were based on data from guinea pig white matter (Table 1). We note that the connective tissue was modeled using an isochoric constitutive formulation within FEBio (Muskoloskeletal Research Laboratory, UT, USA). The neural tissue was modeled as compressible to allow for potential motion of fluid into and out of the neural tissues of the LC. A 3D von Mises distribution with a fiber dispersion factor of two was used to model the angular distribution of the collagen fibers in the LC beams. A more thorough discussion of the material properties used in this model and their influence on the predictions of the model can be found in our recent report.[32] Displacement driven boundary conditions were obtained by linearly interpolating the displacements predicted from the mesoscale models to the locations of nodes on the boundary of

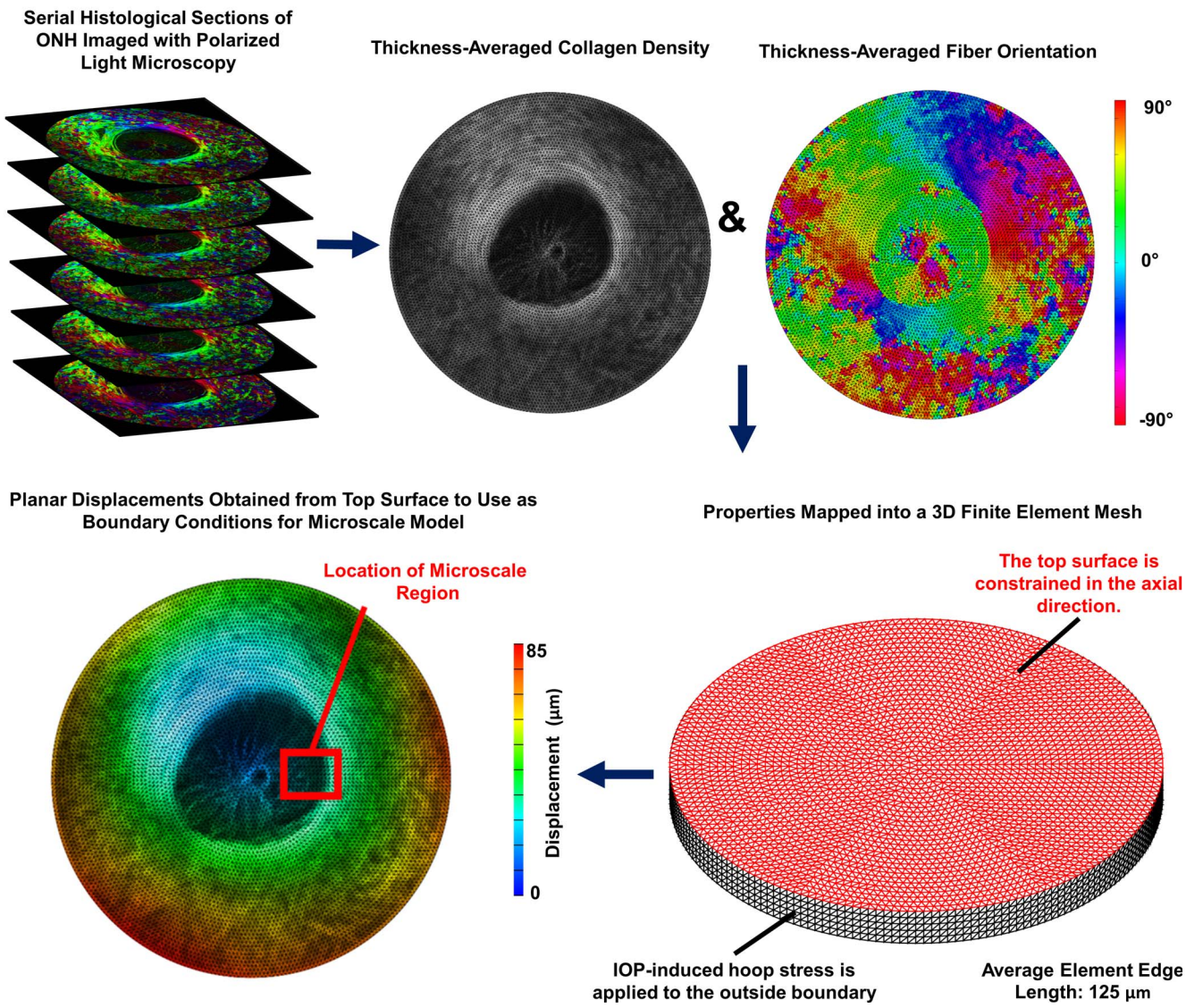

FIGURE 1. Overview of mesoscale modeling approach used to determine boundary conditions for microscale models. Mesoscale models were built from 30-μm thick serial histological image stacks of sheep ONH with 4.4 μm per pixel in-plane resolution. Polarized light microscopy was used to determine the collagen fiber orientation and the local collagen density within each section.[34] Colors in the polarized light microscopy images correspond to the fiber angle. These were mapped onto the finite element mesh and used to determine the stiffness and direction of anisotropy for each element. IOP-induced hoop stress corresponding to 30 mm Hg was applied to the boundary of the model to obtain displacement boundary conditions for the microscale models. The displacements corresponding to the actual location of each microscale model within its corresponding mesoscale model were used. The *red box* shown on the bottom-left image corresponding to the location of the model shown in Figure 2 is shown as an example.

the mesh. Stresses and strains reported herein are for elements along the symmetry surface of the model for which the geometry corresponded directly to the histological image.

Homogenized Models. To study the effects of the LC microstructure, we also constructed a homogenized model of one of the peripheral LC regions for comparison. For the homogenized model, the sclera and lamina (beams and neural tissue together) were segmented at both the mesoscale and microscale levels. The material properties for the sclera at both length scales were chosen to be the same as those used to model the sclera and LC beams. The material properties of the lamina were selected so that the strain energy density was half that of the sclera to account for the lower connective tissue volume fraction of the lamina. The fiber dispersion parameter was set to 0. The displacement data from the mesoscale model under an IOP-induced hoop stress of 30 mm Hg was used as boundary conditions for the microscale homogenized model.

Mechanical Analysis

In this study, we only examine results from the microstructure and homogenized models at the microscale. The first principal and second principal strains and stresses were calculated from the in-plane strain and stress components. The first principal strain represents the largest stretch, whereas the second principal strain represents the stretch in the direction

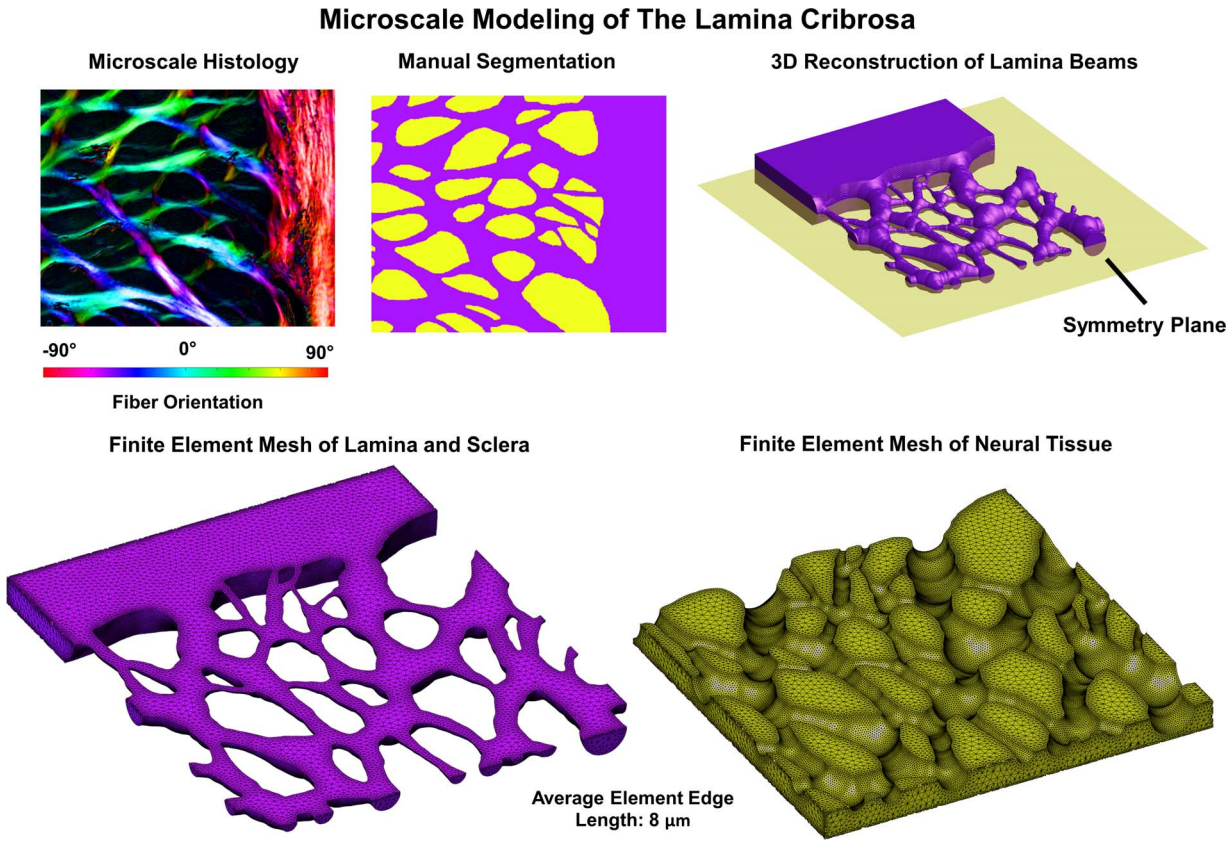

Figure 2. The microstructure models were built from individual sections through the LC and sclera that were reimaged at a higher microscale resolution (0.73 μm per pixel) and registered to the low magnification stacks (see Fig. 1). These models were segmented into LC beams and neural tissues (*top middle*). The segmented images were then used as the basis for a 3D reconstruction of the LC beams (*top right*). Our reconstruction method resulted in beams that were symmetric about a plane through the middle thickness of the reconstructed section. The assumption of symmetry allowed us to model only half of the total reconstructed volume. A finite element model of the beams embedded in neural tissue was then created (*bottom row*). The displacement driven boundary conditions obtained from the mesoscale models was then applied to the microscale model and the deformations of the LC beams, and neural tissues were obtained from the simulation.

orthogonal to the direction of the first principal strain. When both the first and second principal strains are positive, the tissue is in biaxial tension. When both strains are negative, the tissue is in biaxial compression. Shear strain is defined as half of the difference between the first and second principal strains. All stresses and strains are reported with respect to the deformed geometry, with stresses being reported as Cauchy stress in kPa and all strains are reported as Green strain in percent, that is, Green strain multiplied by 100. We calculated the 90th percentile first principal strain using volume-weighted methods as a measure of the peak strain.

Table 1. Material Properties

Connective Tissue	Neural Tissue
Ground substance	Ground substance
Uncoupled Mooney Rivlin	Coupled Mooney Rivlin
C1:150 kPa	C1: 0.876 kPa
C2:0 kPa	C2: 0.614 kPa
K:5000 kPa	K:0.412 kPa
Fiber component	Fiber component
Uncoupled Fiber Exponential Power Law	Coupled Fiber Exponential Power Law
ξ:1600 kPa	ξ:69.4 kPa
α:120	α:1
β: 2	β:2

Analysis of Pore Shape and Size

A total of 128 individual pores fully contained within the seven microstructure models were identified. The following two measures of pore shape were measured: aspect ratio, the ratio of the major to minor axis of the pore, and convexity, the ratio of the area of the pore to the area of the convex hull of the pore (Fig. 3). In addition, the following two measures of pore size were measured: perimeter length and area. Linear mixed effect models controlling for the individual animal and eye from which the models were constructed were tested, but there was not enough variability between the animals and eyes to obtain good fits. Thus, we used multivariate linear regression considering shape and size parameters simultaneously to determine associations between combinations of the shape and size parameters and the 90th percentile tensile strain within a pore. The particular LC region containing the pore was treated as a categorical factor allowing for pores from each region to have different intercepts. This was done so as to control for potential variation due to differences in location and boundary conditions. We tested for associations between the shape and size parameters in both the baseline and deformed configurations. The Akaike information criterion (AIC) was used to determine the best statistical model. Exponential and logarithmic data transforms were tested, but the best fits were found when using untransformed 90th percentile tensile strains.

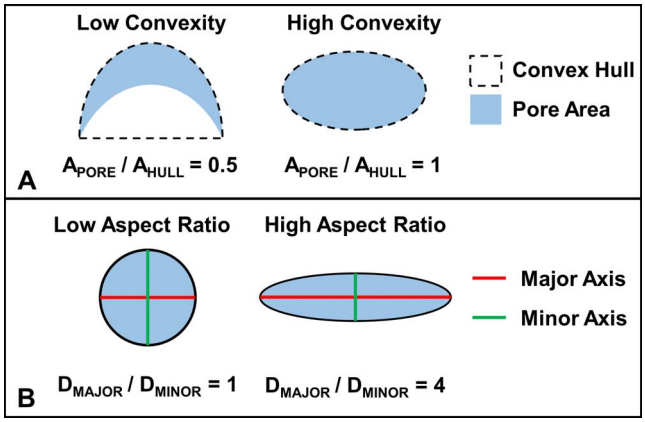

FIGURE 3. (**A**) Convexity is defined using the concept of a convex hull. In mathematical terms, the convex hull of a set of points is the minimum region that fully contains all line segments between any two arbitrary points in the set. From a conceptual standpoint, the convex hull of a polygon would be represented by the shape of a rubber band stretched around the outside of that polygon. In this sense, we can imagine the dashed line surrounding the two pores in the panel to be this rubber band. Specifically, for this study, we defined convexity as the ratio of the area of the pore to the area of the convex hull of the pore. (**B**) Aspect ratio was defined as the ratio of the major axis length to the minor axis length.

Software

FEBio v2.3.0 was used for all finite element analysis.[36] Paintshop Pro X2 (Corel, Ottawa, ON, Canada) was used for manual 2D segmentation of microscale models. Fiji was used for 2D image skeletonization and analysis of polarized light microscopy images including image stitching.[37–39] Custom code and the GIBBON toolbox for Matlab (v2015b; Mathworks, Natick, MA, USA) were used to create mesoscale meshes, generate segmented volumes, register microscale models to mesoscale models, write FEBio input files, analyze data, and measure pore shape.[40] Avizo Wind v8.0.1 (FEI, Hillsboro, OR, USA) was used to register histological sections and create the meshes used to make the microscale models. Linear models were fit and compared using R v3.2.2 (R Foundation for Statistical Computing).[41]

Results

Maps of strains and stress for the microscale homogenized and microstructure models are provided in Figure 4. The first principal strains in the homogenized model were lower and more uniform than those within the neural tissue pores of the microstructure model. The second principal strains in the homogenized model were uniformly positive, indicating pure biaxial tension. In the microstructure model, the second principal strains were often negative, visible in the blue areas in the plot. These represent areas of high compression. Similarly, the shear strains in the microstructure model were much higher than in the homogenized model. The first principal stresses within the homogenized model, similar to the strains, were low and rather uniform as compared to the microstructure model.

When considering combinations of the four baseline shape and size parameters the best model was the combination of convexity, aspect ratio, and area (AIC = –613). Convexity, aspect ratio, and area were all significantly correlated with the peak tensile strain ($P < 0.01$; Table 2). Convexity and area were negatively correlated with the peak tensile strain, whereas aspect ratio was positively correlated. When comparing the normalized slopes, convexity was the most influential factor. Scatter plots of convexity and peak tensile strain with fitted lines for pores from each region are shown in Figure 5. Example pores plotted by convexity and peak tensile strain are shown in Figure 6. The associations between shape and size were also tested using the values from the deformed configuration, as these would represent the shapes observed clinically when IOP is still elevated. The best fit model using the deformed parameters was still the combination of convexity, aspect ratio, and area (AIC = –599). However, when using these parameters only convexity and area were significantly correlated with the 90th percentile first principal strain ($P < 0.01$).

The IOP-induced changes in pore convexity, aspect ratio, and area are shown as a function of the initial pore shape in Figure 7, and the cumulative distributions of the three parameters in the unloaded state and after acute IOP increase are shown in Figure 8. Convexity increased in 119 of the 128 pores, indicating that the pores became rounder and less concave. In pores where the change in convexity was negative, the magnitude of that change was small. The change in aspect ratio was more varied, with 61 pores becoming more elongated and 67 pores becoming more circular. There did not appear to be a trend between the initial aspect ratio of the pore and whether it became more elongated or more circular. Pore area increased in 126 of the 128 pores, and the change in area, as a percentage, was more varied in small pores. The two pores that became smaller were both small pores that experienced high compressive strains.

Discussion

We used multiscale microstructure-aware models of the LC and sclera, with which we were able to predict complex patterns of stretch, compression, and shear within the neural tissues of the LC pores due to IOP-induced hoop stress. There were significant correlations between the area, convexity, and aspect ratio of a pore and the level of biomechanical insult to the neural tissues within the pore. The relationship between pore shape and neural tissue insult was observed when pore shape was measured in either the deformed or undeformed configurations. When deformed by IOP-induced hoop stress, the pores became larger and more convex possibly reducing the risk for further insult.

Homogenized models of the LC have been widely employed to study ONH biomechanics at the gross anatomical level and mesoscale levels.[20,29–31,35,42–44] Our study demonstrates that homogenized models are not suitable for studying the microscale structures of the LC. Our homogenized model did provide reasonable estimates of the average deformation across the whole LC, as the average first principal strain calculated across the whole region was on the order of 1% to 2% for both the two homogenized models and the microstructure model. The homogenized model, however, did not provide a good estimate of the levels or types of deformation within the LC pores and RGC axons when compared with previous experimental studies.[6,7,45] This is important, as strains in the range of 10% to 20% can trigger astrocytic remodeling and neuron damage.[9,10,46] In our microstructure models, the collagen beams of the LC stretch, thin, and bend. This behavior exacerbates the strains within the neural tissue pores, leading to compression and high shear strains. The homogenized model did not predict any in-plane compression, missing a potentially important biomechanical insult. Compressive strains have been hypothesized to contribute to a reduction in axoplasmic transport, another potential mechanism of RGC damage and loss.[8] The homogenized model still included

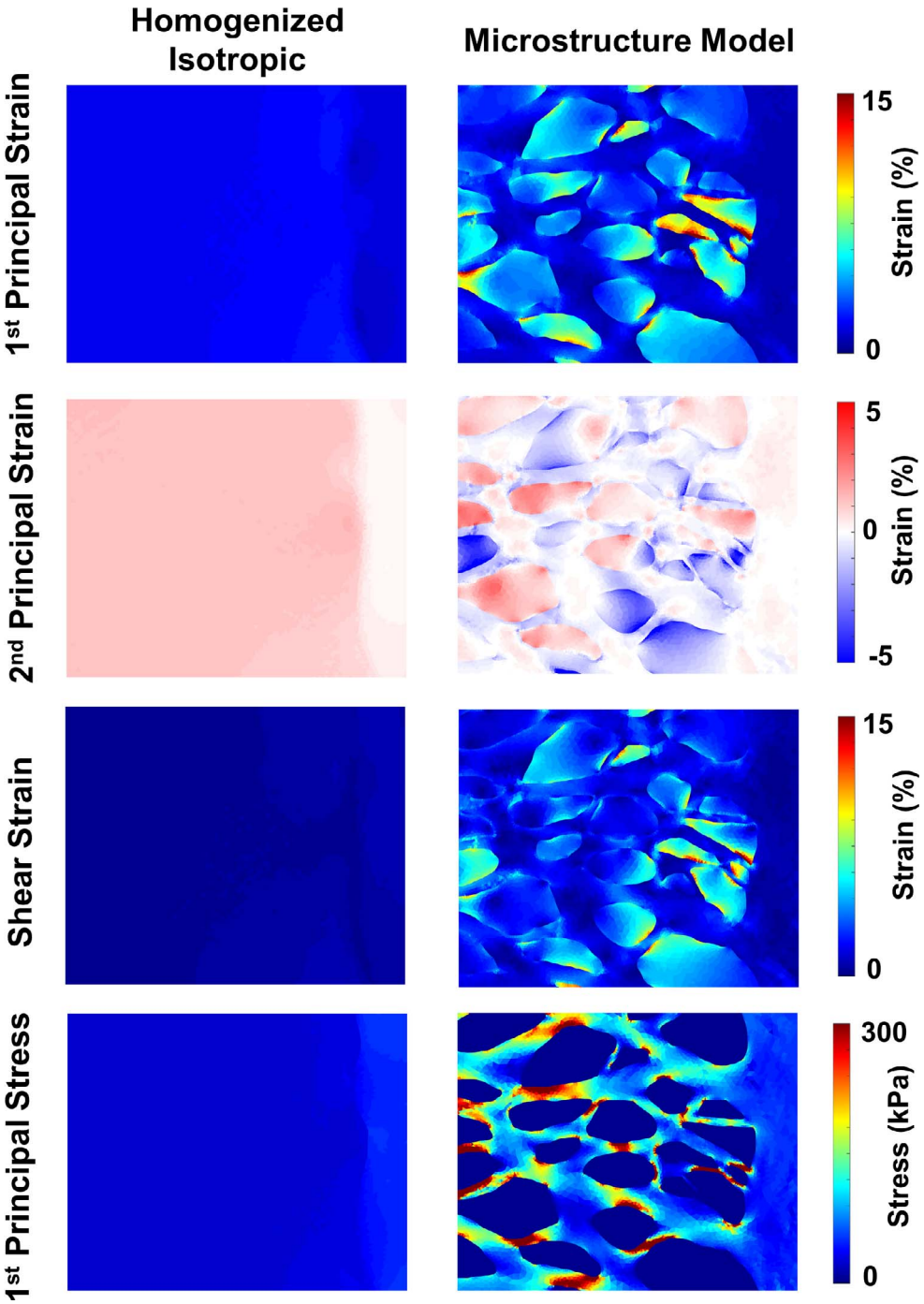

Figure 4. Comparison of strains and stresses between microstructure model and homogenized model. Peak (90th percentile) first principal strains in the microstructure model exceeded 15% as compared to 3% in the homogenized isotropic model (*top row*). The microstructure model predicted in-plane compression in several pores, whereas no compression was observed in the homogenized model (*second row*). Similarly, only the microstructure model predicted high shear strains within the neural tissues (*third row*). Stresses within the lamina beams were much higher than those predicted by the homogenized model and typically concentrated in areas away from the beam intersections regions (*bottom row*).

Table 2. Best Fit Statistical Model for Predicting 90th Percentile First Principal Strain From LC Pore Shape Parameters

Parameter	Slope	Standard Error	*P* Value
Convexity	−48.2	9.79	2.82×10^{-6}
Aspect ratio	0.0871	0.0321	0.00761
Area, μm^2	-1.02×10^{-4}	3.51×10^{-5}	0.00422

mechanical properties based on the collagenous tissue within the LC. If one were to build a model that considered the LC as being entirely composed of neural tissues, we would expect that the deformation would vastly exceed the levels we report here.

Our study suggests that both pore size and pore aspect ratio are important determinants of neural tissue insult with large elongated pores being more prone to high stretch. Convexity had the strongest predictive power. To our knowledge, there

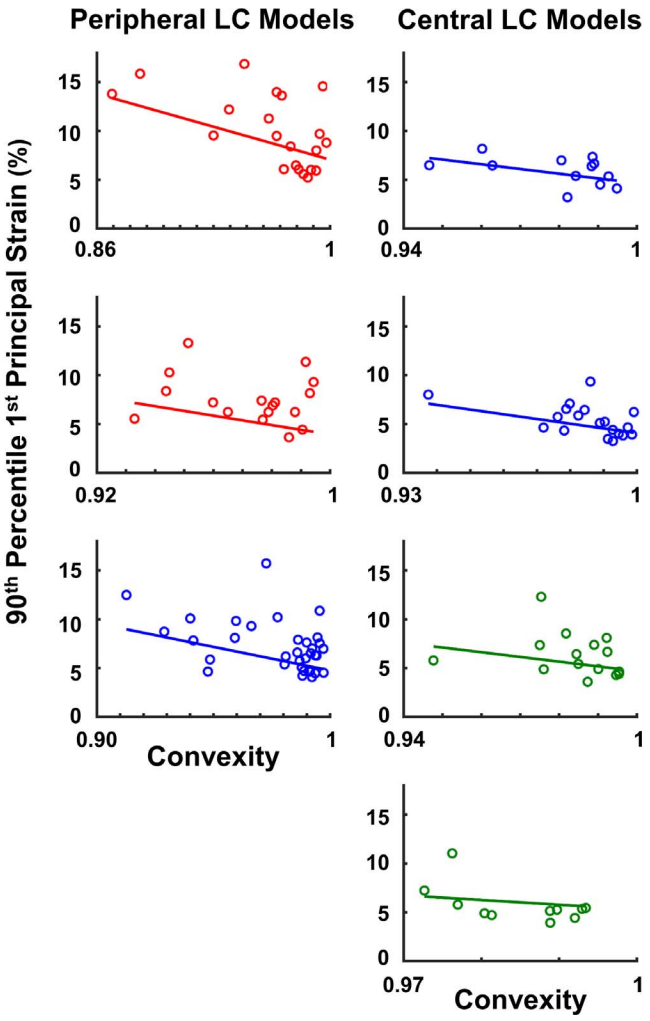

Figure 5. Linear model predictions are shown for each of the seven microstructure models. More convex pores tended to have lower peak tensile strains. Different colors are used to denote regions from different eyes.

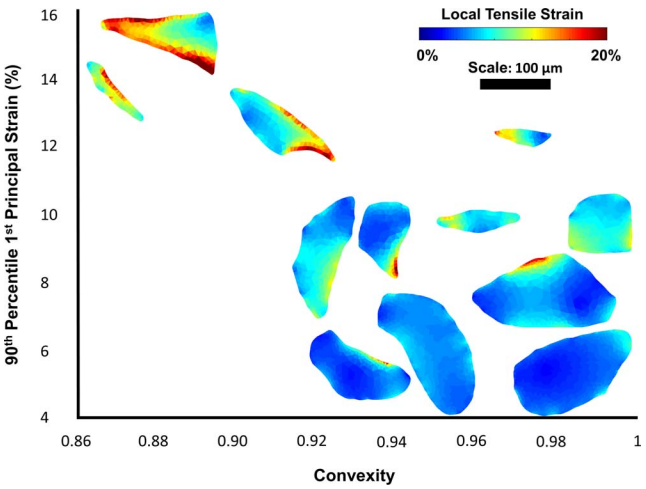

Figure 6. Twelve example pores are plotted by convexity and peak first principal strain. The pores are colored by their local strain maps. Peak strains tend to occur on the concave edges of the pores.

have been no systematic studies on LC pore convexity. Mechanistically, we propose that the high tensile strains within concave pores are due to the straightening of the initially curved beams surrounding the pores under IOP-induced loading. As a curved beam straightens it exerts tension on the pore on the concave edge and compresses the pore on the convex edge. This effect would be smaller or not present along straight beams as these would tend to deform longitudinally. The concept of beam straightening is supported by the fact that the pores in our study almost universally became more convex. Future in vivo studies of LC pore shape may do well to consider convexity in addition to aspect ratio. However, precise measurement of convexity may be a challenge as the resolution and contrast of current in vivo imaging techniques such as OCT are far less than what we obtain with ex vivo microscopy.

In vivo studies testing for associations between the distribution of lamina pore shape and glaucoma status in humans have reported conflicting findings. A study by Akagi et al.[23] found that pores in glaucomatous eyes were significantly larger in area than those from healthy controls, but did not find a significant correlation between aspect ratio and disease status. In glaucomatous eyes, Wang et al.[17] found no significant change in pore area, but instead found a significantly increased variance in pore area. When considering aspect ratio, Miller and Quigley,[18] Fontana et al.,[22] and Zwillinger et al.[24] all measured significantly more elongated pores in glaucomatous eyes. However, these are balanced by the reports of Akagi et al.[23] and Wang et al.,[17] who did not find a significant correlation.

Beyond imaging resolution there are several challenges faced in the clinical measurement and analysis of pore shape. First, pore shape is measured under IOP. For this reason, we tested the associations between pore shape and size with strain using measurements with and without IOP-induced deformation. Although the statistical model using the deformed measurements was not quite as good as the model using the undeformed configuration (AIC = –599 vs. AIC –613), there were still significant associations between pore convexity and area. Another obstacle is the fact that it may be difficult to distinguish the acute shape changes due to IOP from the chronic changes that may occur with disease. Thus, before any measure of pore shape can be considered as a marker of glaucomatous risk, it is necessary to distinguish between the shapes and sizes that lead to higher strains in the LC and the shapes and sizes that result from remodeling due to chronically elevated IOP. A few studies have looked at chronic changes in pore shape.[19,21] Tezel et al.[21] tracked mean pore area and aspect ratio in patient eyes and found that the area of the pores decreased with time, but found no significant change in aspect ratio. Because patients underwent therapy to lower IOP, these changes may not fully reflect the changes that occur with disease. Ivers et al.[19] studied pore area and aspect ratio changes in a monkey model of early glaucoma and found that the area of the pores increased from the baseline condition, but found no significant changes in aspect ratio.

Although we have not studied chronic changes in this work, we have been able to study the acute effects of IOP-induced hoop stress on pore shape. Our findings suggest that pores become larger in area under the influence of IOP-induced hoop stress, which agrees with our in vivo experiments in monkey eyes in which we found that LC pore diameter increases when the translaminar pressure gradient is acutely increased.[47] We also found a similar increase in pore area using second harmonic generation in human eyes during an ex vivo inflation test.[48] We also found that pores became more convex. The distribution of pore aspect ratio in our study was similar in the loaded and unloaded configurations. Thus, on average the measured distribution of pore aspect ratio under IOP-induced

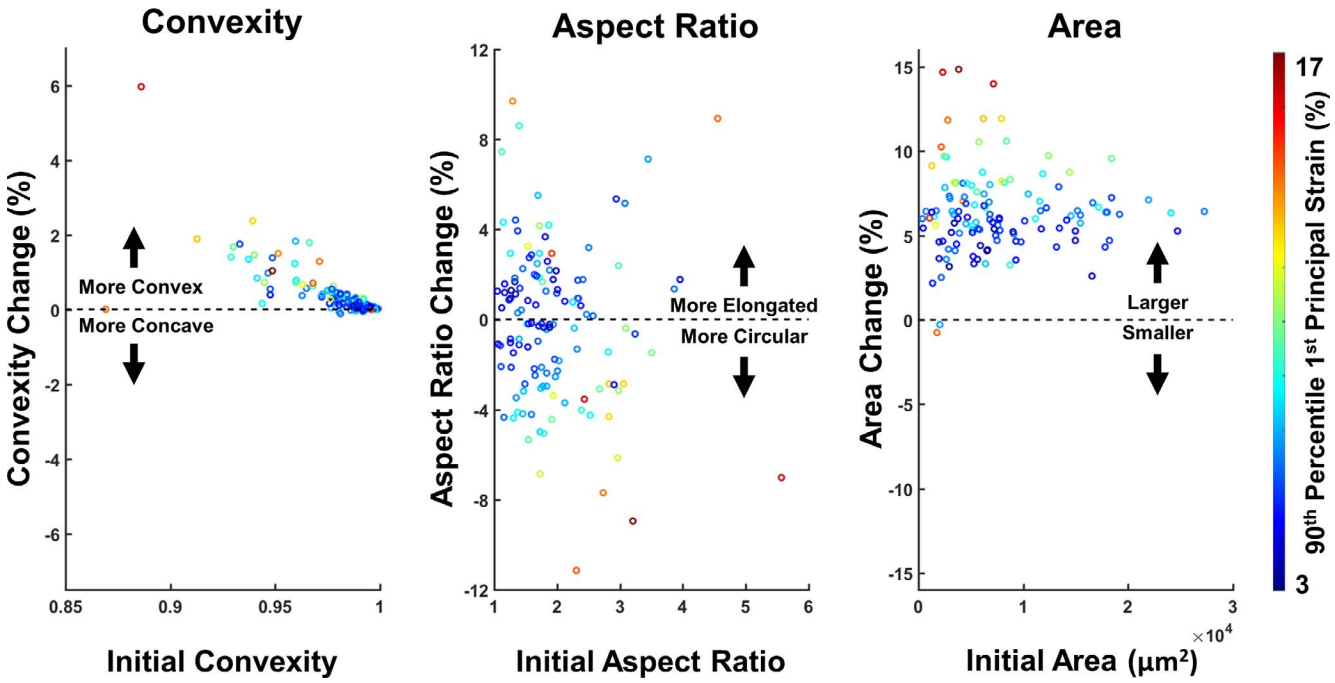

Figure 7. The convexity, aspect ratio, and area of the pores change under acutely elevated IOP. Scatter plots are shown comparing the relative change in shape or size in relationship to the initial state. The color of the data points represents the 90th percentile strain in that pore. Nearly all pores became more convex after elevated IOP, with highly concave pores undergoing the biggest changes and suffering the highest levels of strain. Although the high-aspect ratio was associated with high strains, 48% of the pores became more elongated under elevated IOP and 52% became more circular. All but two pores became larger under elevated IOP, with large changes in area, typically being associated with large strains. There was more variability in area change and tensile strain for small pores as compared to large pores.

hoop stress may well reflect the unloaded distribution, which we have demonstrated is correlated with high tensile strains. However, within this distribution, the pores did change aspect ratio from the baseline condition with roughly half of the pores becoming more elongated and half of the pores becoming more circular. This is important because it highlights the strength of quantifying LC sensitivity to IOP on a pore-by-pore level. If we had only considered the pore aspect ratio distribution we would not have detected important effects of IOP-induced hoop stress.

This high-resolution modeling work was made possible by our development of polarized light microscopy methods for measuring collagen birefringence and alignment at the submicron scale.[33,34] We have elected to make models based on sheep ONH as we have established the robustness of our methods for this animal model. The microstructure of the

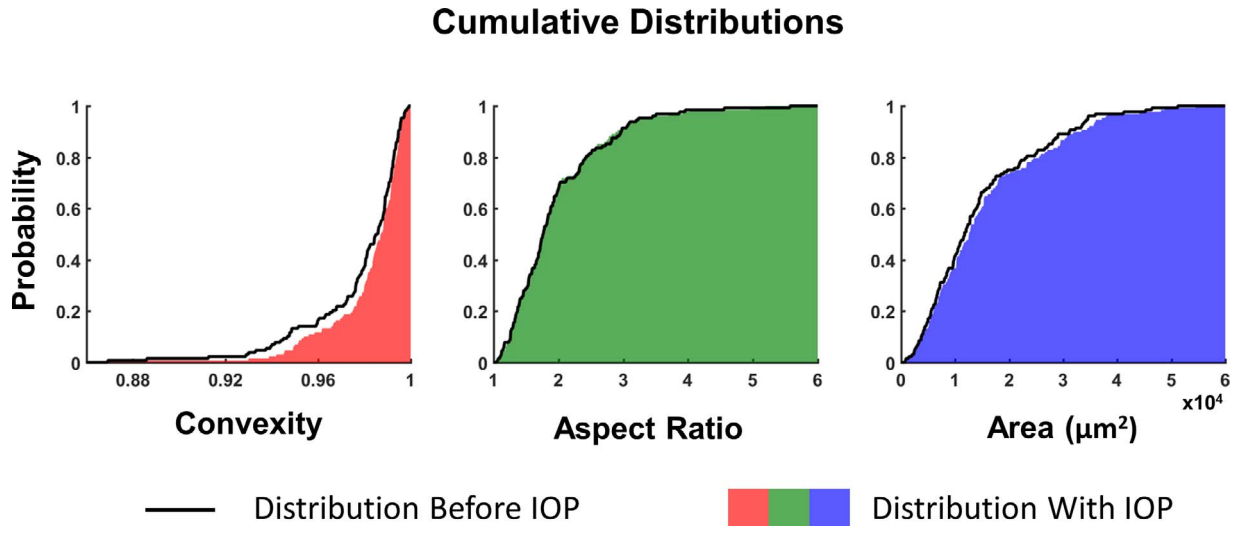

Figure 8. The cumulative distribution of pore shape and size are shown in the initial condition (*black line*) and after elevated IOP (*solid color*). The rightward shift in the distribution of convexity indicates that the deformed pores are more convex after elevated IOP. The distribution of pore aspect ratios was largely unchanged by the increase in IOP. A slight rightward shift of the distribution of pore areas was observed highlighting the increase in pore area under elevated IOP.

Investigative Ophthalmology & Visual Science

human LC is distinct from that of sheep, most notably in the reduced size and increased number of pores. Although the models in this work were based on sheep eyes, the mechanism underlying our findings appears relatively general and therefore it seems plausible that our findings will extend to the human LC. Nevertheless, this must still be validated.

Within this work, we have made some simplifying assumptions about the geometry and mechanics of the LC and sclera. The most notable assumption is the fact that our model is only a planar model. This assumption is justified based on one of the fundamental principal of mechanics, the Law of Laplace, which states that the in-plane stresses in a thin spherical shell will be many times greater than the pressure inside the shell. This assumption is commonly employed in biomechanics[49–52] and in particular ocular biomechanics.[29,53–56] We should note that our use of Laplace's law also assumes that the distribution of hoop-stress is constant across the boundaries of our mesoscale models, ignoring subtle variations due to changes in regional thickness. The advantages and disadvantages of the assumption of planarity have been discussed at length in the work of Zhang et al.[29] Although this assumption means that our models do not capture the effects of the LC curvature, the models still allow us to study the response of the LC to its primary loading without making additional assumptions about the out-of-plane fiber structure. On the positive, though, our shape parameters were also 2D measures, which has the advantage being easily comparable to clinical and experimental findings that are often based on en-face or coronal images.

This study was primarily focused on the effects of LC pore shape and size. In a recent study, we conducted systematic parametric analyses to determine how the properties of the LC beams and neural tissues influence the biomechanical insult within the LC pores.[32] A discussion of the implications of the choice of tissue properties can be found there. For every set of material properties modeled, we still found large focal deformation within the LC pores. However, the distribution of the strains was somewhat dependent on the stiffness of the collagen beams, with stiffer collagen beams leading to a more narrow distribution of strains over the microscale regions. Thus, it seems likely that there are interactions between tissue shape and mechanical properties, as have been noted for much simpler models of the ONH.[57] These interactions must be better understood before extending our findings into clinical practice. We also did not consider the effects of collagen distribution and its interaction with the effects of pore shape; however, our previous study suggested that collagen fiber dispersion had very minor effects on LC pore strain.[32] Another assumption on the material behavior of our models was a stress-free configuration based on the microstructure obtained from eyes that were pressure fixed at 5 mm Hg. This pressure represents a low-stress configuration that does not suffer from potential artifacts that could arise from using unloaded tissues (zero pressure). However, this means that our material properties may be underpredicting the stiffness of the tissues at this initial geometry as they do not consider the stresses caused by the pressure at fixation. Given the fact that the material properties were estimated from literature values and that we have previously found that the deformation of sheep eyes between IOP's of 0 and 10 mm Hg is small when compared with the deformation between 10 and 20 mm Hg,[58] we reasoned that this assumption would have only minor influences on the interpretation of our results. Given the tissue nonlinear mechanical properties, it is possible that the correlation between LC pore shape and IOP will be different for pressure differences other than the 0 and 30 mm Hg studied here. Nonetheless, this study was intended primarily to provide a mechanistic framework for understanding the relationship between LC pore shape and biomechanical insult.

In conclusion, the stiff LC beams lead to large focal concentrations of stretch, compression, and shear in the compliant neural tissues within the LC pores resulting from IOP-induced hoop stress. Homogenized models fail to predict both the magnitudes and type of deformation. The convexity, aspect ratio, and area of a LC pore are strong predictors of the tensile strain within that pore. Under IOP-induced hoop stress, lamina pores tend to become larger and more convex. The knowledge of how LC pore shapes change with elevated IOP will enhance our interpretation of future clinical studies on pore shape and size.

Acknowledgments

The authors thank Emma Chen for assisting with image segmentation and Danielle Hu for assisting in the collection, stitching, and registering of images.

Supported in part by National Institutes of Health Grants R01-EY023966, R01-EY025011, P30-EY008098, and T32-EY017271 (Bethesda, MD, USA), the Eye and Ear Foundation (Pittsburgh, PA, USA), and Canadian Institutes of Health Research (Operating Grant 1234448).

Disclosure: **A.P. Voorhees**, None; **N.-J. Jan**, None; **M.E. Austin**, None; **J.G. Flanagan**, None; **J.M. Sivak**, None; **R.A. Bilonick**, None; **I.A. Sigal**, None

References

1. Elkington AR, Inman CB, Steart PV, Weller RO. The structure of the lamina cribrosa of the human eye: an immunocytochemical and electron microscopical study. *Eye (London, England)*. 1990;4(Pt 1):42–57.
2. Quigley HA, Addicks EM, Green WR, Maumenee AE. Optic nerve damage in human glaucoma. II. The site of injury and susceptibility to damage. *Arch Ophthalmol*. 1981;99:635–649.
3. Sigal IA, Ethier CR. Biomechanics of the optic nerve head. *Exp Eye Res*. 2009;88:799–807.
4. Campbell IC, Coudrillier B, Ross Ethier C. Biomechanics of the posterior eye: a critical role in health and disease. *J Biomech Eng*. 2014;136:021005.
5. Girard MJ, Dupps WJ, Baskaran M, et al. Translating ocular biomechanics into clinical practice: current state and future prospects. *Curr Eye Res*. 2015;40:1–18.
6. Sigal IA, Grimm JL, Jan NJ, Reid K, Minckler DS, Brown DJ. Eye-specific IOP-induced displacements and deformations of human lamina cribrosa. *Invest Ophthalmol Vis Sci*. 2014;55:1–15.
7. Midgett DE, Pease ME, Jefferys JL, et al. The pressure-induced deformation response of the human lamina cribrosa: analysis of regional variations. *Acta Biomater*. 2017;53:123–139.
8. Quigley HA. Reappraisal of the mechanisms of glaucomatous optic nerve damage. *Eye (London, England)*. 1987;1(Pt 2):318–322.
9. Exler RE, Guo X, Chan D, et al. Biomechanical insult switches PEA-15 activity to uncouple its anti-apoptotic function and promote erk mediated tissue remodeling. *Exp Cell Res*. 2016;340:283–294.
10. Rogers RS, Dharsee M, Ackloo S, Sivak JM, Flanagan JG. Proteomics analyses of human optic nerve head astrocytes following biomechanical strain. *Mol Cell Proteomics*. 2012;11:M111.012302.
11. Hernandez MR. The optic nerve head in glaucoma: role of astrocytes in tissue remodeling. *Prog Retin Eye Res*. 2000;19:297–321.

12. Balaratnasingam C, Kang MH, Yu P, et al. Comparative quantitative study of astrocytes and capillary distribution in optic nerve laminar regions. *Exp Eye Res*. 2014;121:11–22.
13. Burgoyne CF. A biomechanical paradigm for axonal insult within the optic nerve head in aging and glaucoma. *Exp Eye Res*. 2011;93:120–132.
14. Ishida T, Jonas JB, Ishii M, Shinohara K, Ikegaya Y, Ohno-Matsui K. Peripapillary areterial ring of Zinn-Haller in highly myopic eyes as detected by optical coherence tomography angiography. *Retina*. 2017;37:299–304.
15. Wang B, Lucy KA, Schuman JS, et al. Decreased lamina cribrosa beam thickness and pore diameter relative to distance from the central retinal vessel trunk. *Invest Ophthalmol Vis Sci*. 2016;57:3088–3092.
16. Nadler Z, Wang B, Schuman JS, et al. In vivo three-dimensional characterization of the healthy human lamina cribrosa with adaptive optics spectral-domain optical coherence tomography. *Invest Ophthalmol Vis Sci*. 2014;55:6459–6466.
17. Wang B, Nevins JE, Nadler Z, et al. In vivo lamina cribrosa micro-architecture in healthy and glaucomatous eyes as assessed by optical coherence tomography. *Invest Ophthalmol Vis Sci*. 2013;54:8270–8274.
18. Miller KM, Quigley HA. The clinical appearance of the lamina cribrosa as a function of the extent of glaucomatous optic nerve damage. *Ophthalmology*. 1988;95:135–138.
19. Ivers KM, Sredar N, Patel NB, et al. In vivo changes in lamina cribrosa microarchitecture and optic nerve head structure in early experimental glaucoma. *PLoS One*. 2015;10:e0134223.
20. Campbell IC, Coudrillier B, Mensah J, Abel RL, Ethier CR. Automated segmentation of the lamina cribrosa using Frangi's filter: a novel approach for rapid identification of tissue volume fraction and beam orientation in a trabeculated structure in the eye. *J R Soc Interface*. 2015;12:20141009.
21. Tezel G, Trinkaus K, Wax MB. Alterations in the morphology of lamina cribrosa pores in glaucomatous eyes. *Br J Ophthalmol*. 2004;88:251–256.
22. Fontana L, Bhandari A, Fitzke FW, Hitchings RA. In vivo morphometry of the lamina cribrosa and its relation to visual field loss in glaucoma. *Curr Eye Res*. 1998;17:363–369.
23. Akagi T, Hangai M, Takayama K, Nonaka A, Ooto S, Yoshimura N. In vivo imaging of lamina cribrosa pores by adaptive optics scanning laser ophthalmoscopy. *Invest Ophthalmol Vis Sci*. 2012;53:4111–4119.
24. Zwillinger S, Paques M, Safran B, Baudouin C. In vivo characterization of lamina cribrosa pore morphology in primary open-angle glaucoma. *J Fr Ophtalmol*. 2016;39:265–271.
25. Sredar N, Ivers KM, Queener HM, Zouridakis G, Porter J. 3D modeling to characterize lamina cribrosa surface and pore geometries using in vivo images from normal and glaucomatous eyes. *Biomed Opt Express*. 2013;4:1153–1165.
26. Ivers KM, Li C, Patel N, et al. Reproducibility of measuring lamina cribrosa pore geometry in human and nonhuman primates with in vivo adaptive optics imaging. *Invest Ophthalmol Vis Sci*. 2011;52:5473–5480.
27. Reynaud J, Lockwood H, Gardiner SK, Williams G, Yang H, Burgoyne CF. Lamina cribrosa microarchitecture in monkey early experimental glaucoma: global change. *Invest Ophthalmol Vis Sci*. 2016;57:3451–3469.
28. Winkler M, Jester B, Nien-Shy C, et al. High resolution three-dimensional reconstruction of the collagenous matrix of the human optic nerve head. *Brain Res Bull*. 2010;81:339–348.
29. Zhang L, Albon J, Jones H, et al. Collagen microstructural factors influencing optic nerve head biomechanics. *Invest Ophthalmol Vis Sci*. 2015;56:2031–2042.
30. Roberts MD, Liang Y, Sigal IA, et al. Correlation between local stress and strain and lamina cribrosa connective tissue volume fraction in normal monkey eyes. *Invest Ophthalmol Vis Sci*. 2010;51:295–307.
31. Sigal IA, Flanagan JG, Tertinegg I, Ethier CR. Modeling individual-specific human optic nerve head biomechanics. Part I: IOP-induced deformations and influence of geometry. *Biomech Model Mechanobiol*. 2009;8:85–98.
32. Voorhees AP, Jan NJ, Sigal IA. Effects of collagen microstructure and material properties on the deformation of the neural tissues of the lamina cribrosa. *Acta Biomater*. 2017;58:278–290.
33. Jan NJ, Lathrop K, Sigal IA. Collagen architecture of the posterior pole: high-resolution wide field of view visualization and analysis using polarized light microscopy. *Invest Ophthalmol Vis Sci*. 2017;58:735–744.
34. Jan NJ, Grimm JL, Tran H, et al. Polarization microscopy for characterizing fiber orientation of ocular tissues. *Biomed Opt Express*. 2015;6:4705–4718.
35. Coudrillier B, Boote C, Quigley HA, Nguyen TD. Scleral anisotropy and its effects on the mechanical response of the optic nerve head. *Biomech Model Mechanobiol*. 2013;12:941–963.
36. Maas SA, Ellis BJ, Ateshian GA, Weiss JA. FEBio: finite elements for biomechanics. *J Biomech Eng*. 2012;134:011005.
37. Schindelin J, Arganda-Carreras I, Frise E, et al. Fiji: an open-source platform for biological-image analysis. *Nat Method*. 2012;9:676–682.
38. Preibisch S, Saalfeld S, Tomancak P. Globally optimal stitching of tiled 3D microscopic image acquisitions. *Bioinformatics*. 2009;25:1463–1465.
39. Zhang TY, Suen CY. A fast parallel algorithm for thinning digital patterns. *Commun Acm*. 1984;27:236–239.
40. Moerman KM. gibbonCode/GIBBON: The Geometry and Image-Based Bioengineering Add-On for MATLAB (Release: Hylobates albibarbis). Available at: https://zenodo.org/badge/latestdoi/93002532.
41. R Core Team. *R: A Language and Environment for Statistical Computing*. Vienna, Austria: R Foundation for Statistical Computing; 2013.
42. Grytz R, Sigal IA, Ruberti JW, Meschke G, Downs JC. Lamina cribrosa thickening in early glaucoma predicted by a microstructure motivated growth and remodeling approach. *Mech Mater*. 2012;44:99–109.
43. Voorhees AP, Grimm JL, Bilonick RA, et al. What is a typical optic nerve head? *Exp Eye Res*. 2016;149:40–47.
44. Girard MJ, Suh JK, Bottlang M, Burgoyne CF, Downs JC. Biomechanical changes in the sclera of monkey eyes exposed to chronic IOP elevations. *Invest Ophthalmol Vis Sci*. 2011;52:5656–5669.
45. Tran H, Grimm J, Wang B, et al. Mapping in-vivo optic nerve head strains caused by intraocular and intracranial pressures. *Proc of SPIE*. 2017;10067:100670B.
46. Salvador E, Burek M, Förster CY. Stretch and/or oxygen glucose deprivation (OGD) in an in vitro traumatic brain injury (TBI) model induces calcium alteration and inflammatory cascade. *Front Cell Neurosci*. 2015;9:323.
47. Wang B, Sigal IA, Smith MA, et al. In-vivo 3D deformation of lamina cribrosa microstructure in response to acute changes in intraocular and cerebrospinal fluid pressures. *Invest Ophthalmol Vis Sci*. 2015;56:3979–3979.
48. Amini R, Grimm JL, Jan N-J, Brown DJ, Sigal IA. Lamina cribrosa pore size increases when human eyes are subjected to acute intraocular pressure elevation. *Invest Ophthalmol Vis Sci*. 2014;55:4249–4249.
49. Voorhees AP, Han HC. A model to determine the effect of collagen fiber alignment on heart function post myocardial infarction. *Theor Biol Med Model*. 2014;11:6.

Investigative Ophthalmology & Visual Science

50. Prange HD. Laplace's law and the alveolus: a misconception of anatomy and a misapplication of physics. *Adv Physiol Educ*. 2003;27:34–40.
51. Jackson FW, Adrain AL, Black M, Miller LS. Calculation of esophageal variceal wall tension by direct sonographic and manometric measurements. *Gastrointest Endosc*. 1999;50: 247–251.
52. Zhong L, Ghista DN, Tan RS. Left ventricular wall stress compendium. *Comput Methods Biomech Biomed Engin*. 2012;15:1015–1041.
53. Chung CW, Girard MJ, Jan NJ, Sigal IA. Use and misuse of Laplace's law in ophthalmology. *Invest Ophthalmol Vis Sci*. 2016;57:236–245.
54. Sander EA, Downs JC, Hart RT, Burgoyne CF, Nauman EA. A cellular solid model of the lamina cribrosa: mechanical dependence on morphology. *J Biomech Eng*. 2006;128:879–889.
55. Palko JR, Morris HJ, Pan X, et al. Influence of age on ocular biomechanical properties in a canine glaucoma model with ADAMTS10 mutation. *PLoS One*. 2016;11:e0156466.
56. Cahane M, Bartov E. Axial length and scleral thickness effect on susceptibility to glaucomatous damage: a theoretical model implementing Laplace's law. *Ophthalmic Res*. 1992; 24:280–284.
57. Sigal IA. An applet to estimate the IOP-induced stress and strain within the optic nerve head. *Invest Ophthalmol Vis Sci*. 2011;52:5497–5506.
58. Voorhees AP, Ho LC, Jan NJ, et al. Whole-globe biomechanics using high-field MRI. *Exp Eye Res*. 2017;160:85–95.

Investigative Ophthalmology & Visual Science